A Combined NMR and Molecular Dynamics Study of the Transmembrane Solubility and Diffusion Rate Profile of Dioxygen in Lipid Bilayers†

M. Sameer Al-Abdul-Wahid,‡,§ Ching-Hsing Yu,‡,|| Ihor Batruch,§ Ferenc Evanics,§ Régis Pomès,||,⊥ and R. Scott Prosser*,§

Department of Chemistry, University of Toronto, UTM, 3359 Mississauga Road, North Mississauga, Ontario, Canada L5L 1C6, Structural Biology and Biochemistry, Hospital for Sick Children, 555 University Avenue, Toronto, Ontario, Canada M5G 1X8, and Department of Biochemistry, University of Toronto

Received February 8, 2006; Revised Manuscript Received July 5, 2006

ABSTRACT: The transmembrane profile of oxygen solubility and diffusivity in a lipid bilayer was assessed by ^{13}C NMR of the resident lipids (*sn*-2-perdeuterio-1-myristelaidoyl-2-myristoyl-*sn*-glycero-3-phosphocholine) in combination with molecular dynamics (MD) simulations. At an oxygen partial pressure of 50 atm, distinct chemical shift perturbations of a paramagnetic origin were observed, spanning a factor of 3.2 within the *sn*-1 chain and an overall factor of 10 from the headgroup to the hydrophobic interior. The distinguishing feature of the ^{13}C NMR shift perturbation measurements, in comparison to ESR and fluorescence quenching measurements, is that the local accessibility of oxygen is achieved for nearly all carbon atoms in a single experiment with atomic resolution and without the use of a probe molecule. MD simulations of an oxygenated and hydrated lipid bilayer provided an immersion depth distribution of all carbon nuclei, in addition to the distribution of oxygen concentration and diffusivity with immersion depth. All oxygen-induced ^{13}C NMR chemical shift perturbations could be reasonably approximated by simply accounting for the MD-derived immersion depth distribution of oxygen in the bilayer, appropriately averaged according to the immersion depth distribution of the ^{13}C nuclei. Second-order effects in the paramagnetic shift are attributed to the collisionally accessible solid angle or to the propensity of the valence electrons in the vicinity of a given nuclear spin to be polarized or delocalized by oxygen. A method is presented to measure such effects. The excellent agreement between MD and NMR provides an important cross-validation of the two techniques.

The transmembrane distribution and associated transport properties of oxygen are fundamental to cellular respiration and key to many basic processes in the cell. Slight changes in the availability of oxygen at certain sites in the cell membrane are thought to trigger a cascade of responses, brought about by oxygen-sensing mechanisms (*1*, *2*). Changes in local oxygen concentrations are also integrally related to ischemia (*3*, *4*), cellular responses to anesthesia (*5*, *6*), photodynamic therapy, and radiation. A key issue in the role of oxygen in many physiological processes is whether its transbilayer permeation is the limiting step in cellular respiration, and if not, might existing channel proteins facilitate oxygen transport. Current understanding of oxygen transport rates and of the transmembrane distribution of both concentration and diffusion rates has come largely from fluorescence (*7*, *8*) and ESR studies (*9*−*11*), though transport can also be effectively measured across lipid monolayers deposited on a working electrode (*12*−*14*). The prevailing opinion, at least in the case of ESR studies of plasma membranes, is that oxygen permeation across the membrane is not the rate-limiting step in respiration (*15*, *16*). The issue of the relative contribution of passive and facilitated diffusion is also of current interest to cell physiologists (*17*, *18*). ESR and fluorescence quenching measurements designed to probe local oxygen concentration and diffusivity usually rely on a relatively large spin-label or fluorophore, which can be attached to either a lipid-like amphiphile or peptide and thus localized over a range of depths in the membrane. Moreover, the sensitivity of ESR and fluorescence is such that the probe molecule can be used at low concentrations. Nevertheless, the possibility that the oxygen concentration and diffusivity are disrupted in the vicinity of the probe cannot be discounted, making it difficult to deduce the precise oxygen concentration and diffusivity profile of the membrane.

We revisit the problem of the solubility of oxygen with immersion depth from the perspective of solution state ^{13}C NMR of the resident bilayer lipids, where we show that distinct chemical shift perturbations of a paramagnetic origin can be simultaneously measured for nearly every carbon nucleus in the lipid without the use of any sterically perturbing probe. The measured effects span an order of magnitude from the lipid headgroup to the hydrophobic interior and a factor of roughly 3 along the length of the

† R.P. thanks CIHR and the Hospital for Sick Children RTC program for funding. R.P. is a CRCP chairholder. R.S.P. acknowledges support from the American Chemical Society (PRF AC Grant 376620) and the Natural Sciences and Engineering Research Council of Canada (NSERC). R.S. also acknowledges support from the Petroleum Research Council and NSERC.

* To whom correspondence should be addressed. E-mail: sprosser@utm.utoronto.ca. Tel: (905) 828-3802. Fax: (905) 828-5425.

‡ The two first authors contributed equally to this work.

§ Department of Chemistry, University of Toronto.

|| Hospital for Sick Chidren.

⊥ Department of Biochemistry, University of Toronto.

10.1021/bi060270f CCC: $33.50
Published on Web 08/09/2006

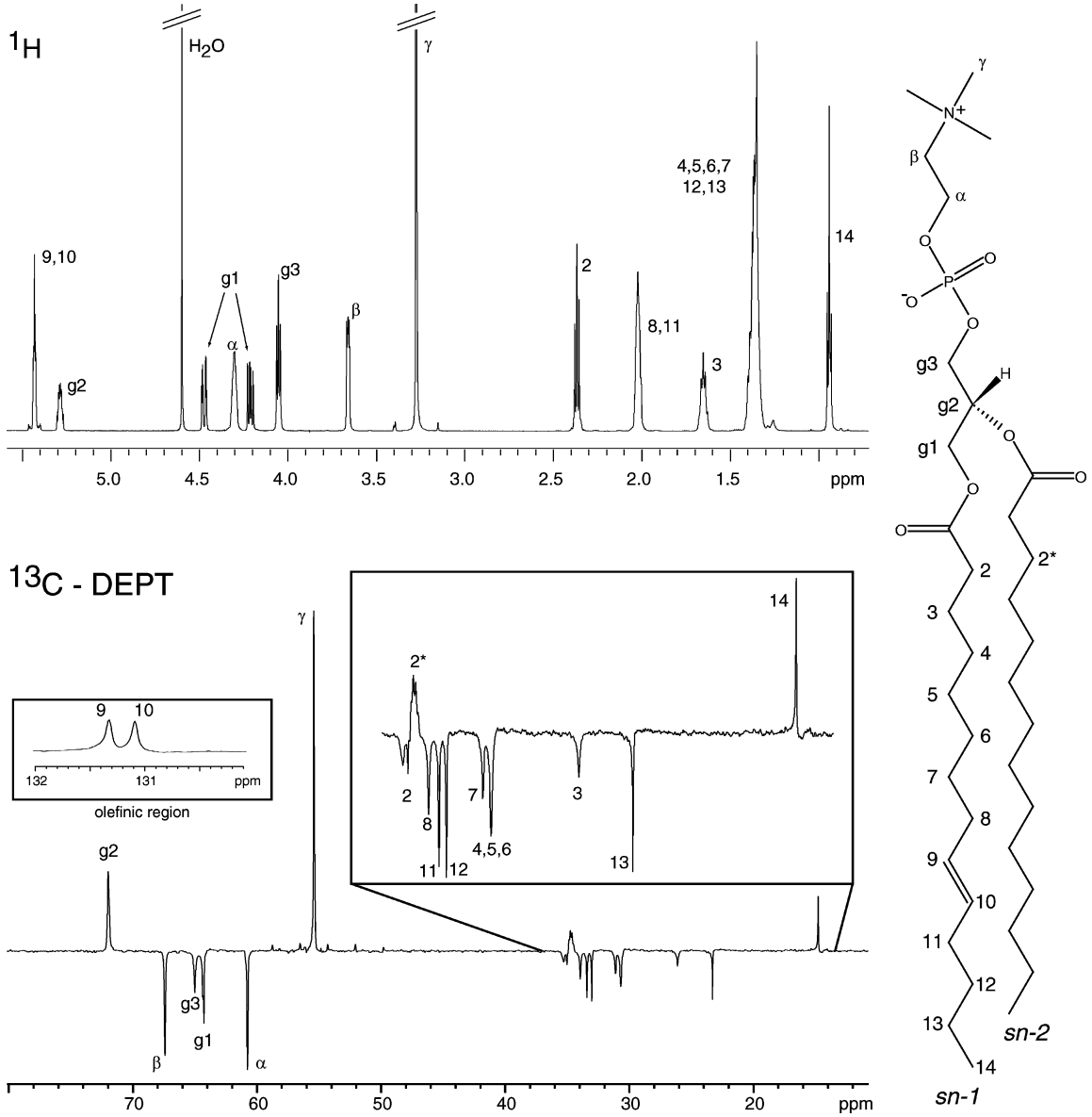

FIGURE 1: Structural formula of MLMPC with corresponding ^{1}H and ^{13}C DEPT NMR spectra at 45 °C. The ^{1}H spectrum is that of MLMPC in 1:1 deuterated methanol/chloroform, while the ^{13}C spectrum is obtained from a 25% (w/w) $q = 0.8$ bicelle mixture of chain-perdeuterated DHPC-d_{22} and MLMPC. ^{1}H and ^{13}C NMR assignments, shown in the figure, were based on literature values and on ^{1}H,^{13}C HSQC and two-bond ^{1}H,^{13}C HMBC experiments.

sn-1 chain of the lipid. Our results are corroborated by molecular dynamics (MD) simulations of oxygen in a fully hydrated lipid bilayer. We discuss herein aspects of the lipid bilayer model system and associated solution NMR experiments followed by an introduction to the theory related to paramagnetic shifts from a diffusible paramagnet and a discussion of the MD simulations.

Atomic Resolution of Lipid Bilayers. Phospholipids present a significant challenge to the NMR spectroscopist due to line broadening and severe overlap of methylene resonances, particularly in multilamellar lipid bilayer aggregates which form spontaneously upon addition of excess water. An alternative model membrane system is the isotropic or fast tumbling bicelle. Bicelles consist of both long-chain phospholipids, which spontaneously form a stable lipid bilayer, and short-chain phospholipids, designed to coat the hydrophobic edges of the disk-shaped bilayer domain, resulting in an aggregate which is considerably smaller than a multi- or unilamellar vesicle. The small aggregate size facilitates rapid tumbling of the bicelle in solution, giving rise to relatively narrow line widths in the associated NMR spectra (*19*, *20*). To further eliminate the overlap of methylene resonances, we have made use of an unsaturated phospholipid, *sn*-2-perdeuterio-1-myristelaidoyl-2-myristoyl-*sn*-glycero-3-phosphocholine (MLMPC).[1] The double bond in the *sn*-1 chain of MLMPC improves chemical shift dispersion, and deuteration of the *sn*-2 chain simplifies the resulting spectra, which show peaks resulting only from the *sn*-1 chain. When MLMPC is combined with equimolar amounts of a short-chain lipid (DHPC-d_{22}), the above fast-tumbling bi-

[1] Abbreviations: MLMPC, *sn*-2-perdeuterio-1-myristelaidoyl-2-myristoyl-*sn*-glycero-3-phosphocholine; DHPC, 1,2-dihexanoyl-*sn*-glycero-3-phosphocholine; DMPC, 1,2-dimyristoyl-*sn*-glycero-3-phosphocholine; DOPC, 1,2-dioleoyl-*sn*-glycero-3-phosphocholine; DOPM, 1,2-dioleoyl-*sn*-glycero-3-phosphomethanol; MLEV, Malcolm Levitt's composite pulse decoupling; DEPT, distortionless enhancement by polarization transfer; INEPT, insensitive nuclei enhanced by polarization transfer; HSQC, heteronuclear single-quantum correlation; HMBC, heteronuclear multiple-bond correlation.

celles spontaneously form (*19*, *20*). The structure and assigned ^{1}H and ^{13}C NMR spectra of the long-chain lipid, MLMPC, are shown in Figure 1.

Paramagnetic Effects. Paramagnetic effects of oxygen may include local spin−lattice relaxation (T_1), line broadening (T_2), and chemical shift perturbations. The majority of NMR studies involving oxygen as a paramagnetic probe have utilized T_1 or T_2 effects on ^{1}H nuclei to study protein topology and protein−protein interactions (*21*−*27*). The paramagnetic influence of oxygen on T_1 and T_2 is relatively easy to interpret, in part because the oxygen electronic spin relaxation times are sufficiently short (on the order of picoseconds) to render the effective correlation time associated with modulation of the dipolar interaction constant (*28*). A second consequence of the short electronic relaxation time is that line broadening is relatively weak at partial pressures where significant paramagnetic spin−lattice relaxation rates and chemical shift perturbations are observed (i.e., 20−50 atm).

This paper focuses on oxygen-induced paramagnetic shifts, rather than spin−lattice relaxation effects, to study permeation of oxygen in lipid bilayers. This approach has the advantage that the effects are directly related to local oxygen concentrations, while one need not be concerned with deuteration levels and the effects of spin diffusion, which often complicate ^{1}H relaxation rate analyses, particularly in membranes and micelles. Small ^{1}H chemical shift perturbations from oxygen have been previously reported in protein studies (*23*), and sizable oxygen-induced ^{19}F chemical shift perturbations have been reported and used to study membrane immersion depth (*29*) and protein topology (*30*). In the latter study, a site-directed spin-labeling approach was taken, in which a cysteine-specific fluorinated substituent was employed so that relative differences in oxygen-induced paramagnetic shifts could be interpreted in terms of membrane protein structure and environment. In the present case, our goal is to directly measure local effects of oxygen in a lipid bilayer without the use of any probe molecule. We observe that modest partial pressures (50 atm) are sufficient to observe significant ^{13}C NMR paramagnetic shifts, which we attribute to a contact mechanism (*31*). Contact shifts, which arise from unpaired electron spin density at the resonant nucleus, are typically awkward to compute or interpret in terms of structural information (*32*, *33*). Contact shifts arising from a freely diffusible paramagnet might be expected to be even more complicated. However, here we adopt a very empirical approach and assume the paramagnet does not undergo strong binding at or near the nucleus of interest (i.e., does not coordinate with a specific geometry), in which case the key variables may simply involve the local oxygen concentration, $[O_2]$, and the depth distribution function of the probe nucleus, ρ_i. This situation is distinct from either ESR or fluorescence spectroscopy, where the collisional frequency of oxygen, which involves both $[O_2]$ and the local diffusion coefficient, D_{O_2}, dictates the magnitude of quenching. The characteristic frequency associated with a diffusional jump is much faster than the NMR time scale, in which case the chemical shift perturbations should be determined by the average time an oxygen molecule is associated with a given carbon nucleus. In other words, we expect that the paramagnetic shifts should relate to the local oxygen concentration rather than the product of the concentration and oxygen−carbon collision frequency. For the moment we consider both cases: (1) the strong collision limit, in which the contact shift depends on the collisional frequency of the paramagnet with the ^{13}C atom (i.e., the product of the oxygen concentration and diffusion coefficient, D_{O_2}) (*9*), and (2) the weak collision limit where the paramagnetic shifts will depend on the local oxygen concentration in the membrane. Under the assumption of the strong collision limit, we express the ^{13}C contact shift, $\Delta\delta_i$, acting on nucleus i, resulting from nonspecific collisional accessibility of oxygen, as

$$\Delta\delta_i = k\int \rho_i(z)[O_2(z)]D_{O_2}(z)\,dz \qquad (1a)$$

where k is simply a proportionality constant and the integral accounts for the variation of the local oxygen concentration, $[O_2(z)]$, and diffusion coefficient, $D_{O_2}(z)$, with immersion depth, z, weighted by the depth-dependent distribution function of the ith nucleus, $\rho_i(z)$. Here we approximate the collisional frequency by the product of the oxygen concentration and diffusion coefficient, and we neglect any contribution from lipid diffusion or translational excursions resulting from acyl chain isomerizations. The alternative description of the contact shift neglects diffusion as discussed above, in which case we define an appropriate proportionality constant, k', and we write

$$\Delta\delta_i = k'\int \rho_i(z)[O_2(z)]\,dz \qquad (1b)$$

In either case, to deconvolve the above contributions, we have performed an all-atom molecular dynamics (MD) simulation of a hydrated lipid bilayer, involving the lipid MLMPC, in the presence of oxygen and under conditions approximating those used in our experiment. The MD simulations provide an independent assessment of $\rho_i(z)$, $[O_2(z)]$, and $D_{O_2}(z)$, leaving only the global proportionality constant, k', as an adjustable parameter in the fitting of the paramagnetic shift profile for the entire membrane.

MATERIALS AND METHODS

Sample Preparation. sn-2-Perdeuterio-1-myristelaidoyl-2-myristoyl-*sn*-glycero-3-phosphocholine (MLMPC) and chain-perdeuterated 1,2-dihexanoyl-*sn*-glycero-3-phosphocholine (DHPC-d_{22}) were obtained as powders from Avanti Polar Lipids (Alabaster, AL). Bicelles in which the long-chain to short-chain lipid molar ratio, q, was 0.8 were prepared by first combining dry MLMPC to a stock solution of 25% (w/w) DHPC-d_{22} in D_2O, maintained at pH 7.0 with 100 mM phosphate buffer. An appropriate amount of buffer was subsequently added to obtain a 25% (w/w) dispersion. A few minutes of gentle vortexing was sufficient to obtain a clear mixture. In the study of lipid shift perturbations below the critical concentration for aggregation, approximately 25 mg of MLMPC was solubilized in 700 μL of a 1:1 (molar ratio) deuterated methanol/chloroform solution.

NMR Experiments. All NMR experiments were performed on a 600 MHz Varian Inova spectrometer and a standard HX broad-band probe. In the case of oxygen paramagnetic rate measurements, the sample was usually pressurized in a 5 mm o.d. sapphire NMR tube (Saphikon, NH) to 50−70 atm of oxygen partial pressure for 2 days to speed up equilibration rates and then equilibrated in the magnet while maintaining the desired final pressure of 50 atm. Spectra were

compared to those obtained under equivalent partial pressures of N_2 to factor out any pressure-induced shifts. Absolute referencing of the chemical shift was established through the Varian "setref" macro which establishes a ^{13}C chemical shift based on the lock signal; identical transmitter frequencies were used in both the oxygenated and unoxygenated samples in order to obtain an absolute change in chemical shift from oxygen. Typical ^{13}C and ^{1}H (decoupling) pulse lengths were 7 and 10 μs, respectively, while most spectra were obtained using 500−1200 scans and a repetition time of either 8.2 or 1.4 s, for either ambient or oxygenated membranes. All ^{13}C natural abundance NMR spectra were obtained using a DEPT sequence, which simply converts proton magnetization to transverse ^{13}C magnetization, through two INEPT periods, thereby discriminating between CH, CH_2, and CH_3 groups, while filtering out ^{13}C resonances directly associated with deuterated moieties. Thus, only ^{13}C NMR aliphatic signals from the *sn*-1 chain of the long-chain lipid are observed in a ^{1}H-coupled ^{13}C NMR experiment. To optimize resolution, while minimizing local heating due to decoupling, ^{13}C acquisition times were usually 140 ms, under 2500 Hz B_1 decoupling fields and using broad-band MLEV decoupling. Spectral analysis and peak deconvolution were performed using Varian software.

^{13}C Chemical Shift Assignments. Returning to the ^{13}C NMR DEPT spectrum of MLMPC in Figure 1, note that the lipid headgroup resonances arise from both MLMPC and chain-perdeuterated DHPC-d_{22}, since both possess identical phosphatidylcholines. The aliphatic signal arises purely from the long-chain lipid with the exception of the residual signal from the C2 carbon of DHPC-d_{22}, which is not fully deuterated at this position. The headgroup and glycerol backbone resonances are well established for both ^{1}H and ^{13}C NMR. However, the majority of aliphatic resonances of the *sn*-1 chain of MLMPC are also resolvable in the ^{13}C spectrum, due to the fact that the 9,10 trans double bond causes additional chemical shift dispersion in the so-called plateau region of the lipid chain and in part to relatively long T_2 relaxation times of this model system. The *sn*-2 chain is perdeuterated and, thus, not observed. Assignments were obtained by a combination of ^{1}H,^{13}C HSQC and HMBC experiments where both one- and two-bond scalar couplings (i.e., $^{1}J_{CH}$ and $^{2}J_{CH}$ couplings of 145 and 10 Hz) were utilized.

Molecular Dynamics Simulations. The CHARMM program (*34*), version 27, was used for the simulations of oxygen diffusion in MLMPC bilayers. The CHARMM22 force field (*35*, *36*), TIP3P water potential (*37*), and Lennard-Jones dioxygen potential (*38*) were used to model the system. Calculations were carried out under experimental conditions, i.e., 318 K and 1 atm and, upon bilayer equilibration, constant N, P_N, γ, and T, which denote the number of particles, normal pressure, surface tension, and temperature of the ensemble, respectively. At the early stage of bilayer equilibration, elevated temperatures and N, P_N, A, T (where A denotes constant surface area) were used. The Langevin piston algorithm (*36*) was used to maintain the pressure and surface tension using a piston mass of 500 amu, a collision frequency of 10 ps^{-1}, and a surface tension of 10 dyn/cm (see below). Temperature was maintained using the Hoover thermostat (*39*). Periodic boundary conditions and tetragonal symmetry were applied to the lipid systems. The particle-mesh Ewald (PME) method (*40*) was employed to calculate the electrostatic interactions with a κ value of 0.3 and a grid spacing of approximately 1 Å for the three-dimensional fast Fourier transform. Nonbonded pair lists were updated heuristically with a cutoff of 14 Å for the real-space portion of the Ewald sum and the Lennard-Jones potential, which was smoothly switched off to zero over the range of 10−12 Å. The SHAKE algorithm (*41*) was used to fix the length of all covalent bonds involving hydrogen. The time step for the integration of the equations of motion was 2 fs.

The initial MLMPC bilayer was constructed from 32 all-trans lipids (16 per monolayer) placed on a regular grid; 1152 water molecules were then added to the system, yielding a stoichiometry of 36 water molecules per lipid. This system was then subjected to several hundred picoseconds of N, P_N, A, T simulations with a surface area per lipid set to either 62.3 or 68.5 $Å^2$ and with temperatures ranging from 318 to 500 K. The resulting preequilibrated bilayers were then inspected, and three systems were separately chosen for replication to a full 128 lipid model system. Each of these three bilayer systems was subjected to further equilibration for at least 500 ps, followed by 2 ns of N, P_N, γ, T simulation at 318 K with a surface tension of 10 dyn/cm; 128 oxygen molecules were then introduced to the middle of the water layer (64 per side) on a regular grid. Each model system was then subjected to a final 8 ns N, P_N, γ, T calculation. The last 2 ns of these trajectories was used for analysis. A separate 5 ns simulation of a neat bilayer was performed as a reference.

The optimal value of the applied surface tension was determined from simulations at three different strengths, 10, 15, and 20 dyn/cm. Recent work by Sankararamakrishnan and Weinstein (*42*) suggested that a value of 25−30 dyn/cm should be used for a system of 90 DMPC lipid molecules. In this study, a surface tension of 10 dyn/cm was chosen because it led to a surface area per lipid of 63.3 ± 1.3 $Å^2$ at 318 K (average of 2 ns simulations) in good agreement with experimental DMPC bilayer measurements of 60.0 and 65.4 $Å^2$ at 303 and 323 K, respectively (*43*). The equilibration of the lipid systems was further verified on the basis of bilayer thickness and order parameters, which are in good agreement with experimental and MD results (*42*, *43*). The partitioning of O_2 from the water layer to the bilayer interior required over 4 ns of simulation time. Equilibration was assumed once the number of O_2 molecules within the hydrophobic interior of the bilayer reached a steady state (i.e., the numbers of O_2 molecules entering and exiting the bilayer over a period of 100 ps became approximately equal).

Calculating Oxygen Concentrations and Diffusion Coefficients. The distribution of oxygen concentration (with respect to immersion depth) was evaluated from the simulations as the number of oxygen molecules in the local volume of a 2 Å slice along the bilayer normal. To obtain reliable statistics, the distributions were determined by sampling 600 conformations from 60 trajectories at 10 ps intervals. The local diffusion coefficients of O_2 in the bilayer plane, D_{xy}, with respect to immersion depth were calculated through the slope of the mean-square displacement (MSD):

$$D_{xy}(z) = \frac{1}{4t} \lim_{t \to \infty} \langle |r(t) - r(0)|^2 \rangle \qquad (2)$$

where $[r(t) - r(0)]^2$ is the displacement in the bilayer xy plane at time t.

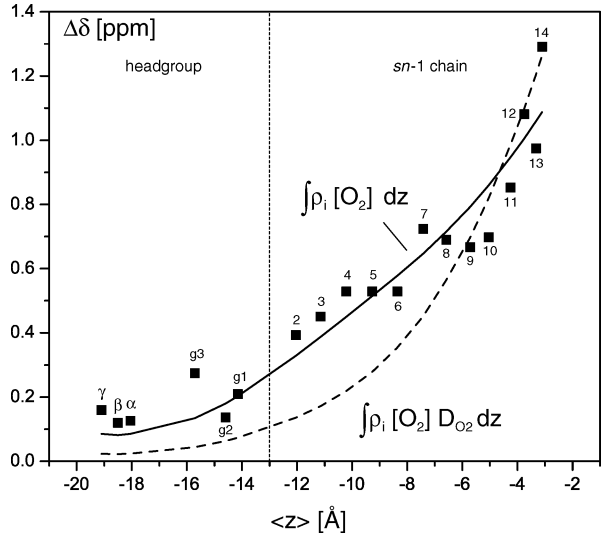

FIGURE 2: Oxygen-induced ^{13}C chemical shift perturbations, $\Delta\delta_i$, of MLMPC in a $q = 0.8$ bicellar mixture at 45 °C. Shift perturbations were determined by subtracting the chemical shifts of the assigned ^{13}C NMR DEPT spectrum of MLMPC under oxygen from the equivalent spectrum under nitrogen. Note that resonances assigned to carbon nuclei 4−6 overlap. Therefore, only an average shift perturbation can be determined for these three resonances. Two fits to $\Delta\delta_i$ in the lipid bilayer are shown: one based on an MD average involving $\Delta\delta_i = k'\int\rho_i(z)[O_2(z)]\,dz$, shown by the solid line, and the other based on MD incorporating the oxygen diffusion rate, $\Delta\delta_i = k\int\rho_i(z)[O_2(z)]D_{O_2}(z)\,dz$, shown by the dashed line.

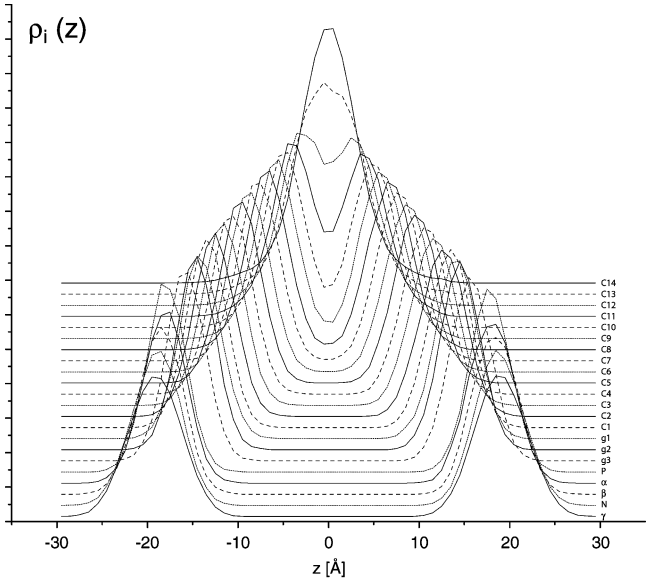

FIGURE 3: Immersion depth distribution profile of carbon nuclei from the *sn*-1 chain of MLMPC, resulting from a 5 ns molecular dynamics simulation involving 128 lipids, 4608 water molecules, and 128 oxygen molecules. Distributions are vertically displaced for clarity, and $z = 0$ is defined to represent the hydrophobic center of the bilayer.

A slab of 2 Å was used for the evaluation, and the slabs were moved along the *z*-axis in 1 Å increments to obtain the coefficients at different depths. To improve statistics, the time origin, $t = 0$, was assigned independently for each O_2 molecule when it entered the slab. Due to the nature of oxygen diffusion, it is not possible to calculate the diffusion coefficients in a finite slab over an infinite time. In this study, the choice of relatively thin slabs forced the calculation of diffusion coefficients over short time intervals of 1−1.6 ps. Longer time intervals (*44*, *45*) could be attained by using thicker slabs. However, this would yield less localized values.

Another method to calculate the diffusion coefficients is to use the force autocorrelation function of O_2 molecules (*43*−*45*). However, this method would require additional simulations with spatial restraints on oxygen positions. Since the primary objective of the MD simulations is to compute the local oxygen concentration and diffusion solubility product, $[O_2(z)] \times D_{O_2}(z)$, the MSD approach, which involves a large number of unconstrained O_2 molecules, offers the advantage of simultaneously yielding the two quantities of interest, $[O_2(z)]$ and $D_{O_2}(z)$.

RESULTS AND DISCUSSION

Transmembrane ^{13}C Paramagnetic Shift Effects from Oxygen. Figure 2 depicts the oxygen-induced ^{13}C chemical shift perturbations for nuclei spanning the entire bilayer (i.e., headgroup and hydrophobic domain) at a partial pressure of 50 atm. Shift perturbations, $\Delta\delta_i$, were determined by subtracting the chemical shifts of the assigned ^{13}C NMR DEPT spectrum of MLMPC under nitrogen from those under the equivalent pressure of oxygen. Note that resonances assigned to carbon nuclei 4, 5, and 6 overlap, and therefore only an average shift perturbation can be determined for these three nuclei. Overall, the paramagnetic shifts span an order of magnitude across the entire bilayer, while the shifts associated with the *sn*-1 chain span a factor of 3.2 from carbon 2 to the terminal methyl carbon. Dashed and solid lines represent fits based upon eqs 1a and 1b (vide infra). We consider next the various contributions to the paramagnetic shifts based on a thorough MD analysis of the identical lipid bilayer.

Calculations of the Solubility and Diffusivity from Molecular Dynamics Simulations. Figure 3 displays the immersion depth distribution functions of carbon nuclei belonging to the *sn*-1 chain of MLMPC, obtained from the MD simulations of the lipid bilayer at 318 K. The instantaneous depths of each nucleus are referenced to the plane associated with the hydrophobic center of the bilayer. Therefore, out-of-plane dynamics and intramolecular motions both contribute to the observed distribution of immersion depths. The small magnitude of asymmetry of each distribution with respect to $z = 0$ indicates that statistical convergence is adequate. Note that the glycerol carbons are relatively closely packed and serve to anchor the lipid acyl chains at one end, while the gauche−trans isomerizations of the acyl chain give rise to a prominent disorder gradient along the immersion depth axis (*46*). This disorder is manifested in an increasingly broader distribution of immersion depth toward the methyl terminus of the lipid chain. Similar positional distributions have been measured in oriented lipid bilayers, by a combination of low-angle X-ray and neutron scattering (*47*). As discussed below, the MD-derived immersion depth distributions of the probe (carbon) nuclei must be combined with depth-specific oxygen concentration before the oxygen-induced shift profile can be predicted, using eq 1b.

Figure 4A displays both the oxygen distribution function, $[O_2(z)]$, and diffusion coefficient profile, $D_{O_2}(z)$, determined from the MD simulation. Note that the oxygen concentration is normalized so that the local concentration in the bulk water region roughly agrees with that expected for water in the

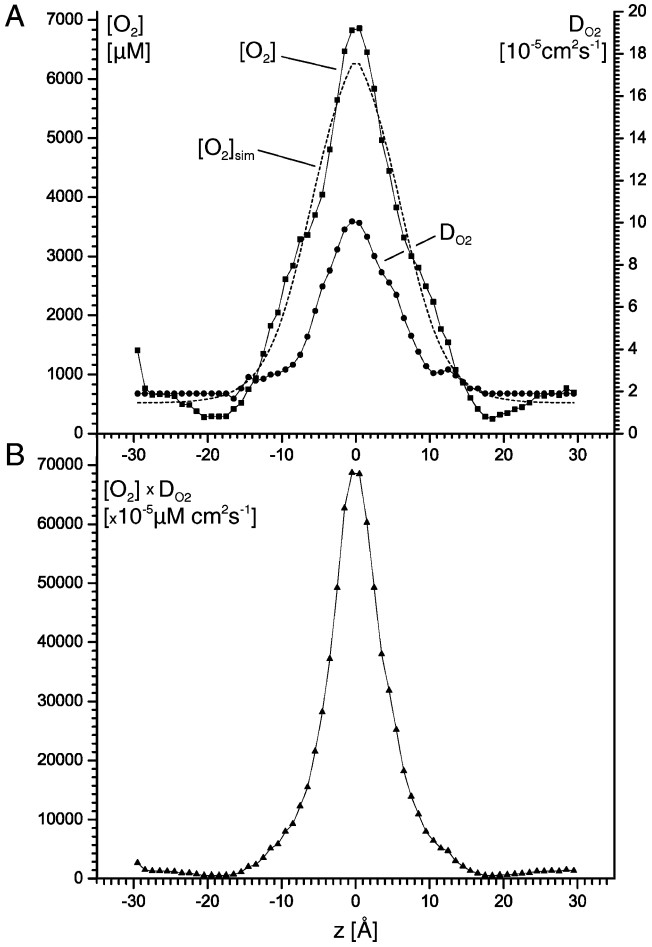

FIGURE 4: (A) Oxygen concentration, $[O_2(z)]$, and diffusion rate, $D_{O_2}(z)$, as a function of immersion depth, based on MD simulations of an MLMPC lipid bilayer at 315 K. Note that the concentration, $[O_2(z)]$, is normalized to that expected at an oxygen partial pressure (P_{O_2}) of 1 atm. The dashed line associated with the oxygen solubility data is a fit to a Boltzmann sigmoidal expression, which describes a simple two-phase distribution of oxygen between water and the membrane interior. (B) The product of the oxygen concentration and diffusion rate versus immersion depth, based on the above MD simulation.

presence of 100 mM salt, assuming an oxygen partial pressure (P_{O_2}) of 1.0 atm (i.e., 800 μM). Since oxygen solubility in the membrane/water system depends linearly on pressure, at least below oxygen partial pressures of 50 atm (*48*), the local concentration can be estimated in this pressure range by multiplying the appropriate value in Figure 4A by the applied oxygen partial pressure. Local oxygen solubility is dictated by hydrophobicity and accessible free volume. As such, it is not surprising that the MD simulation predicts a significant variation in oxygen solubility with immersion depth, since a gradient of accessible free volume is known to exist (*44*). Comparing the difference between the maximum oxygen concentration at $z = 0$ Å (the bilayer center) and that in bulk water, we estimate the excess free energy to be -5.8 kJ/mol, while the average membrane oxygen concentration resulting from the MD simulation translates into an excess free energy of -3.0 kJ/mol at 45 °C. This value is less than the average excess free energy of oxygen in the membrane of -4.5 kJ/mol, computed by Marrink and Berendsen (*44*), although the latter calculation was performed with a saturated lipid at a considerably higher temperature (77 °C). Classic oil/water partitioning experiments of oxygen have suggested an excess free energy on the order of -3.7 kJ/mol (*49*).

The above MD-derived profile of oxygen solubility may be contrasted with that predicted by simple thermodynamic partitioning theory, in which a two-phase distribution between membrane regions with $z < z_0$ and $z > z_0$ is established as a result of the difference in free energy between oxygen in water and in the hydrophobic interior of the membrane (*50*). The Boltzmann sigmoidal distribution, extending from bulk water ($z = -30$ Å) to the bilayer center ($z = 0$ Å) is expressed as

$$[O_2(z)]_{sim} = \frac{[O_2]^{water} - [O_2]^{max}}{1 + \exp[(z - z_0)/\lambda]} + [O_2]^{max} \qquad (3)$$

where oxygen concentrations range from a minimum in bulk water, $[O_2]^{water}$, to a maximum, $[O_2]^{max}$, in the hydrophobic bilayer center. z_0 designates an immersion depth where the oxygen gradient is greatest, while λ characterizes the effective width of the distribution function. The dashed line in Figure 4A represents a fit of eq 3 to the solubility profile determined by MD simulations. In our case, the fitted oxygen concentrations range from $[O_2]^{water} = 520 \pm 100$ μM to a maximum concentration of 7.1 mM in the bilayer center, while λ and z_0 are estimated to be $\lambda = 3.0 \pm 0.25$ Å and $z_0 = -6.11 \pm 0.27$ Å. ESR studies have made use of spin-labeled phospholipid analogues to assess the collisional accessibility of oxygen for the majority of sites, at least in the membrane hydrophobic interior (*9*−*11*, *50*, *51*). These studies reveal a similar value for z_0 although λ is slightly lower than that determined in our case.

Since our focus in this study is to assess the oxygen solubility and diffusivity across the entire bilayer and in the absence of any external probe, we will rely heavily on the MD simulations to connect the solubility profile and carbon depth distribution functions with the resulting paramagnetic chemical shift profile. Examining Figure 4A, a comparison of the MD $[O_2]$ profile (solid squares) to the sigmoidal approximation (dotted line) shows that the MD profile is different in several respects from that predicted by partition theory. For example, oxygen concentrations and mobilities in the vicinity of the glycerol headgroup are observed to be lower than that in bulk water (Figure 4A), and the depth-dependent oxygen concentration profile exhibits a slight inflection in the vicinity of the (trans) double bond. Such subtleties are no doubt a result of local density effects, void volumes, and local lipid dynamics, all of which are incorporated in the MD approach.

Figure 4A also displays the MD-derived oxygen diffusion coefficients as a function of average immersion depth (solid circles), where the diffusion coefficient is predicted to increase in the hydrophobic interior by a factor of 5 compared to that in the bulk water phase, with an average diffusion coefficient of 3.7×10^{-5} cm^2 s^{-1} (at 318 K). This result compares favorably with the average diffusion coefficient predicted by Marrink and Berendsen for a DPPC lipid bilayer at 350 K (*44*), which may be extrapolated to be 4×10^{-5} cm^2 s^{-1} at 318 K, assuming Arrhenius behavior and an activation energy of 4.4 kJ/mol. Moreover, experimental estimates of oxygen diffusion coefficients in tetradecane are on the order of 3.4×10^{-5} cm^2 s^{-1} at 296 K (*52*). Clearly,

accurate estimations of both the concentration and diffusion coefficient of oxygen with atomic resolution are necessary to predict the oxygen collisional frequency with the probe species. At issue is the nature of the effect of oxygen on the ^{13}C chemical shifts; in the event that the oxygen encounters are in the strong collision limit, the chemical shift perturbations should depend on the product of the diffusion coefficient and concentration, shown in Figure 4B. On the other hand, as discussed earlier, in the weak collision limit the paramagnetic gradient should depend on the oxygen concentration profile, as shown in Figure 4A. To assess the validity of the predicted oxygen concentration profile and collisional frequency profile, we must next consider the motions and exact distribution of immersion depth of each of the carbon nuclei in the lipid, as introduced in eqs 1a and 1b.

Evaluating the Oxygen-Induced Chemical Shift Perturbation Profile. We now revisit the paramagnetic shift perturbations shown in Figure 2 in an attempt to explain the data on the basis of the above MD analysis. The dashed line represents theoretical contact shifts calculated using eq 1a [which incorporates the carbon immersion depth distribution, oxygen concentration profile, and oxygen diffusion coefficient profile, i.e., $\Delta\delta_i = k\int\rho_i(z)[O_2(z)]D_{O_2}(z)\,dz$], while the solid line represents theoretical shifts calculated using eq 1b, which assumes that the shifts are determined solely by the oxygen concentration profile and carbon immersion depth distribution, i.e., $\Delta\delta_i = k'\int\rho_i(z)[O_2(z)]\,dz$. In either case, only a single adjustable parameter (k or k') is used to fit the entire chemical shift perturbation profile. Clearly, the solid line associated with eq 1b reproduces the observed paramagnetic shifts remarkably, confirming that the oxygen diffusion profile does not play a significant role in affecting the ^{13}C NMR paramagnetic shift trend.

Second-Order Effects. Although the paramagnetic shifts seem to be well represented by $\Delta\delta_i = k'\int\rho_i(z)[O_2(z)]\,dz$, we consider next whether slight departures from the curve might arise due to second-order effects. We consider two effects: a polarizing correction factor, α_i, associated with the propensity of the local valence electrons to be delocalized or polarized, and a steric term, which we express as the correction factor associated with the average collisionally accessible solid angle at the nucleus of interest, $\langle\Omega_i\rangle$.

Due to differences in delocalization and polarizability, we expect a difference in response to a diffusible paramagnet acting on sp^1-, sp^2-, or sp^3-bonded carbon nuclei (*53*), which we incorporate into α_i. For example, the sp^3 orbitals of the aliphatic carbons of the *sn*-1 chain all extend further from the nucleus, owing to higher p-orbital content, than those of the sp^2 orbitals of carbon atoms 9 and 10, (the trans double bond). Curiously, $\Delta\delta_i$ does indeed appear to fall below the predicted line for C9 and C10, associated with the sp^2 orbitals, as shown in Figure 2. This "susceptibility" effect, which we refer to as α_i, could be assessed if an experiment could be performed under conditions where the lipid was exposed to a uniform oxygen profile. Such an experiment was attempted by first dissolving the lipid in a 1:1 methanol/chloroform solution, below the critical micelle concentration. Oxygen-induced chemical shift perturbations were then measured in a manner identical to that performed in bicelles (included in Supporting Information), and shifts associated with C9 and C10 were observed to be approximately 20% less than those of the carbons in the immediate vicinity of the double bond, C8 and C11. Such a correction (i.e., $\alpha_9 = \alpha_{10} = 1.2$) would indeed place the paramagnetic shifts very near the fitted (solid) line in Figure 2. We have recently taken a similar approach in a separate study of solvent accessibility by dioxygen-induced ^{13}C chemical shift perturbations of a soluble protein, observed via ^1H,^{13}C HSQC spectra (*54*). In this case, the observed paramagnetic shift for each ^{13}C species in the protein was divided by the shift observed for the equivalent ^{13}C atom from the free amino acid. Thus, potential variations in the sensitivity of ^{13}C paramagnetic shifts due to delocalization or polarizability effects from nearby oxygen can be accounted for.

Another potential source of second-order effects might arise from steric protection, which we express in terms of a collisionally accessible solid angle correction factor, $\langle\Omega_i\rangle$. For example, the penultimate carbon may experience additional protection from the bulky terminal methyl group, giving rise to a slightly lower shift perturbation, $\Delta\delta_{13}$, as is seen in Figure 2. Indeed, the shift of the penultimate carbon is also about 20% lower than $\Delta\delta_{12}$ or $\Delta\delta_{14}$ in the methanol/chloroform sample, suggesting a correction factor of $\langle\Omega_{13}\rangle = 1.2$.

Combining both of these second-order effects with eq 1b provides the following equation for the theoretical paramagnetic shift:

$$\Delta\delta_i = k''\alpha_i\langle\Omega_i\rangle\int\rho_i(z)[O_2(z)]\,dz \qquad (4)$$

where α_i and $\langle\Omega_i\rangle$ are determined from experiments where $[O_2(z)]$ is constant for all z.

Note that eq 4 is intended to apply only to a freely diffusing paramagnet, such as oxygen, in which we envisage the polarizing factor, α_i, to be an isotropic average. Similarly, the collisionally accessible solid angle is assumed to be weakly correlated with the various lipid conformations such that it may be separately considered from the integral in eq 4. Finally, a key assumption is that the local oxygen solubility does not depend on the instantaneous lipid conformation. In principle, the MD simulations could provide the solubility profile associated with each member of the ensemble of lipid conformers, thereby avoiding this assumption. However, encounters with molecular oxygen for certain nuclei are quite rare. Consequently, very long MD trajectories would be necessary to sample a statistically meaningful average of oxygen distributions for each carbon nucleus within the vast ensemble of lipid conformations. The above notwithstanding, the quality of the fit of the solid line in Figure 2 suggests that these assumptions are reasonable and that the corrections introduced by considering second-order effects are relatively small.

Caveats in the Bicelle Model. A bicelle membrane model was necessary to achieve the requisite resolution in this study. The morphology of the isotropic bicelle has been carefully considered by neutron scattering, light scattering, and ^{31}P NMR (*55*). This and other studies have confirmed that the combination of a 14-C and 6-C phosphatidylcholine (i.e., DMPC and DHPC, respectively) formed an aggregate in which the two lipids were demixed (i.e., a bicelle rather than a mixed micelle), for long-chain to short-chain lipid molar ratios (q) between 0.25 and 1.0. On the basis of these results we can estimate that, for a $q = 0.8$ bicelle, the radius, R, of

the bilayer "disk" in the plane of the membrane is no more than 70 Å (*55*, *56*). This dimension implies that a given bicelle aggregate consists of not more than 500 MLMPC molecules, where we would expect a significant fraction to be in contact with the DHPC interface. Therefore, extrapolation of the present results to an infinite bilayer devoid of DHPC must be viewed with caution until the effect of the DHPC boundary lipids can be considered in greater detail. More recently, we have studied the distribution of oxygen-induced paramagnetic shifts of MLMPC in small unilamellar vesicles (unpublished results). In this case, the oxygen paramagnetic shift trend is similar. In general, the ESR results portray a comparable paramagnetic gradient across the hydrophobic region of the membrane. Dzikovski et al. recently observed ESR line shapes and oxygen-induced changes in line width and T_{1e} of spin-labeled lipid analogues, spanning a factor of 2 in DMPC bilayers at 30 °C (*11*). Using a spin-labeled α-helical peptide, Nielsen et al. reported electronic spin−lattice relaxation times, T_{1e}, to span a factor of 2.3 and 2.6 across the hydrophobic domain of DOPC and DOPM bilayers, respectively (*57*). However, it should be pointed out that their conclusion regarding the oxygen diffusion coefficient profile is considerably different than the result obtained in our simulations, which predict that oxygen diffuses significantly faster in the hydrophobic interior, in comparison to water. Conflicting results on relative oxygen diffusion coefficients in the hydrophobic interior have been reported (*44*, *45*). This discrepancy is due at least in part to systematic errors in the estimates of diffusion rates in bulk water. Systematic differences between various models of water yield self-diffusion coefficients that differ by a factor of 2.

CONCLUSION AND FINAL REMARKS

In this study we have revisited the oxygen accessibility profile in a lipid bilayer, previously studied in detail by ESR and fluorescence quenching experiments, via ^{13}C solution NMR, where we have demonstrated that atomic resolution can be achieved and the local accessibility of oxygen can be measured without the use of bulky or sterically perturbing probes. MD simulations of the identical MLMPC lipid bilayer provided an estimation of the transmembrane distributions of the carbon nuclei of interest, $\rho_i(z)$, the local oxygen concentration profile, $[O_2(z)]$, and the local oxygen diffusion coefficient profile, $D_{O_2}(z)$. An equation was proposed to quantitatively explain the observed paramagnetic shifts for a diffusible uncharged paramagnet. To first order, this equation proposes that the shift perturbation, $\Delta\delta_i$, may be approximated by the integral involving the oxygen concentration, weighted by the transmembrane distribution function of the probe nucleus. The MD-derived integral, $\int \rho_i(z)[O_2(z)]\, dz$, was found to be in excellent agreement with the observed ^{13}C shift perturbations across the entire bilayer. Moreover, by comparing simulations which assumed that the paramagnetic shift was due either to the concentration of oxygen or to the collisional frequency $[O_2(z)] \times D_{O_2}(z)$, we confirmed that, in the case of ^{13}C NMR, oxygen interactions are essentially in the weak collision limit and that variations in the diffusion rate may be neglected. Second-order corrections involving both the propensity of a given nuclear spin to be delocalized and/or polarized, α_i, in addition to corrections associated with differences in the collisionally accessible solid angle at the nucleus of interest, $\langle\Omega_i\rangle$, were considered. By preparing the lipid in a solvent in which it did not aggregate, and where the oxygen concentration was assumed to be homogeneous, it was noted that the paramagnetic shifts associated with the two sp^2-hybrized carbon nuclei, C9 and C10, were less than the shifts of the neighboring sp^3-hybridized C8 and C11 nuclei. This was attributed to the property that valence electrons of C9 and C10 are less easily delocalized by oxygen, although it is possible that oxygen accessibility is also slightly lower in the vicinity of the olefinic carbon nuclei, due perhaps to lower void volume in the vicinity of the trans double bond. It was also noted that the shift associated with the penultimate carbon, C13, was slightly lower than that of C12 or C14, possibly due to the protective effect of the C14 methyl group. Corrections associated with C9, C10, and C13, based on measurements obtained from MLMPC in 1:1 methanol/chloroform solution, were noted to bring these data points essentially along the fitted solid line shown in Figure 2. It is important to emphasize that the MD simulations were accomplished independently from the NMR experiments, in order that both approaches might be evaluated according to the degree to which they provided a consistent description of the oxygen solubility profile. Remarkably, this excellent agreement provides an important cross-validation of the two techniques and demonstrates that the approximations inherent in the theoretical model (eq 1b) as well as those in the molecular mechanics force field and the methodology of the simulations of hydrated bilayers are essentially correct.

The study of oxygen permeation in lipid bilayers and cells has been significantly advanced by both fluorescence quenching and ESR studies using labels attached to amphiphiles at various immersion depths. The distinct advantage of the current ^{13}C NMR study is that the oxygen-induced contact shifts are simultaneously observed on all resolvable ^{13}C nuclei, in complete absence of any sterically perturbing external probe. This is particularly important in the vicinity of the glycerol carbons where the oxygen concentration is determined to be lowest, and therefore diffusion in this region is the rate-limiting step for overall passive oxygen transport. Measurements by either fluorescence or ESR in this region of the membrane are impossible since lipid packing would be disrupted by the reporter group. Given the considerable variation in oxygen concentration and diffusion rates, due presumably to somewhat subtle changes in free volume and hydrophobicity, some caution is warranted in interpreting quenching effects from a bulky reporter group.

Thus far, oxygen-induced paramagnetic shifts have been reported for ^{15}N, ^{1}H, ^{19}F, and ^{13}C NMR, though only for the case of ^{13}C and ^{19}F NMR are the shifts of sufficient magnitude to be of practical utility. One might envisage a similar approach to the study of oxygen-induced ^{13}C chemical shift perturbations in proteins for purposes of studying collisionally accessible surface area and hydrophobicity. In the case of proteins or polymers, which generally possess a distinct, well-packed hydrophobic core, shifts would be anticipated to strongly depend on collisionally accessible solid angles.

ACKNOWLEDGMENT

Our sincere thanks to Prof. Robert G. Bryant for insightful comments.

SUPPORTING INFORMATION AVAILABLE

^{13}C paramagnetic shifts of MLMPC in a 1:1 chloroform/methanol solution. This material is available free of charge via the Internet at http://pubs.acs.org.

REFERENCES

1. Adams, H., Blanco, J. L. J., Chessari, G., Hunter, C. A., Low, C. M. R., Sanderson, J. M., and Vinter, J. G. (2001) Quantitative determination of intermolecular interactions with fluorinated aromatic rings, *Chem. Eur. J. 7*, 3494−3503.
2. Talley, E. M., Sirois, J. E., Lei, Q. B., and Bayliss, D. A. (2003) Two-pore-domain (KCNK) potassium channels: Dynamic roles in neuronal function, *Neuroscientist 9*, 46−56.
3. Spaide, R. F., Armstrong, D., and Browne, R. (2003) Choroidal neovascularization in age-related macular degeneration—What is the cause?, *Retina J. Retinal Vitreous Dis. 23*, 595−614.
4. Zaugg, M., and Schaub, M. C. (2003) Signaling and cellular mechanisms in cardiac protection by ischemic and pharmacological preconditioning, *J. Muscle Res. Cell Motil. 24*, 219−249.
5. Yamada, A., Tanaka, E., Niiyama, S., Yamamoto, S., Hamada, M., and Higashia, H. (2004) Protective actions of various local anesthetics against the membrane dysfunction produced by in vitro ischemia in rat hippocampal CA1 neurons, *Neurosci. Res. 50*, 291−298.
6. Kim, D. (2005) Physiology and pharmacology of two-pore domain potassium channels, *Current Pharm. Des. 11*, 2717−2736.
7. Chalpin, D. B., and Kleinfeld, A. M. (1983) Interaction of fluorescence quenchers with the normal-(9-anthroyloxy) fatty-acid membrane probes, *Biochim. Biophys. Acta 731*, 465−474.
8. Dumas, D., Muller, S., Gouin, F., Baros, F., Viriot, M. L., and Stoltz, J. F. (1997) Membrane fluidity and oxygen diffusion in cholesterol-enriched erythrocyte membrane, *Arch. Biochem. Biophys. 341*, 34−39.
9. Windrem, D. A., and Plachy, W. Z. (1980) The diffusion-solubility of oxygen in lipid bilayers, *Biochim. Biophys. Acta 600*, 655−665.
10. Vrijmoed, L. L. P., Hyde, K. D., and Jones, E. B. G. (1996) *Melaspilea mangrovei sp nov*, from Australian and Hong Kong mangroves, *Mycol. Res. 100*, 291−294.
11. Dzikovski, B. G., Livshits, V. A., and Marsh, D. (2003) Oxygen permeation profile in lipid membranes: Comparison with transmembrane polarity profile, *Biophys. J. 85*, 1005−1012.
12. Ivanov, I. I., Fedorov, G. E., Gus'kova, R. A., Ivanov, K. I., and Rubin, A. B. (2004) Permeability of lipid membranes to dioxygen, *Biochem. Biophys. Res. Commun. 322*, 746−750.
13. Borden, M. A., and Longo, M. L. (2004) Oxygen permeability of fully condensed lipid monolayers, *J. Phys. Chem. B 108*, 6009−6016.
14. Morton, C. J., Pugh, D. J. R., Brown, E. L. J., Kahmann, J. D., Renzoni, D. A. C., and Campbell, I. D. (1996) Solution structure and peptide binding of the SH3 domain from human Fyn, *Structure 4*, 705−714.
15. Subczynski, W. K., Hyde, J. S., and Kusumi, A. (1989) Oxygen permeability of phosphatidylcholine cholesterol membranes, *Proc. Natl. Acad. Sci. U.S.A. 86*, 4474−4478.
16. Subczynski, W. K., Hopwood, L. E., and Hyde, J. S. (1992) Is the mammalian-cell plasma-membrane a barrier to oxygen-transport, *J. Gen. Physiol. 100*, 69−87.
17. Beckwith, J., Tjepkema, J. D., Cashon, R. E., Schwintzer, C. R., and Tisa, L. S. (2002) Hemoglobin in five genetically diverse Frankia strains, *Can. J. Microbiol. 48*, 1048−1055.
18. Chakraborty, S., Balakotaiah, V., and Bidani, A. (2004) Diffusing capacity reexamined: relative roles of diffusion and chemical reaction in red cell uptake of O-2, CO, CO_2, and NO, *J. Appl. Physiol. 97*, 2284−2302.
19. Vold, R. R., Prosser, R. S., and Deese, A. J. (1997) Isotropic solutions of phospholipid bicelles: A new membrane mimetic for high-resolution NMR studies of polypeptides, *J. Biomol. NMR 9*, 329−335.
20. Luchette, P. A., Vetman, T. N., Prosser, R. S., Hancock, R. E. W., Nieh, M. P., Glinka, C. J., Krueger, S., and Katsaras, J. (2001) Morphology of fast-tumbling bicelles: a small angle neutron scattering and NMR study, *Biochim. Biophys. Acta 1513*, 83−94.
21. Teng, C. L., and Bryant, R. G. (2000) Experimental measurement of nonuniform dioxygen accessibility to ribonuclease a surface and interior, *J. Am. Chem. Soc. 122*, 2667−2668.
22. Hernandez, G., Teng, C. L., Bryant, R. G., and LeMaster, D. M. (2002) O-2 penetration and proton burial depth in proteins: Applicability to fold family recognition, *J. Am. Chem. Soc. 124*, 4463−4472.
23. Ulmer, T. S., Campbell, I. D., and Boyd, J. (2002) The effects of dissolved oxygen upon amide proton relaxation and chemical shift in a perdeuterated protein, *J. Magn. Reson. 157*, 181−189.
24. Ulmer, T. S., Ramirez, B. E., Delaglio, F., and Bax, A. (2003) Evaluation of backbone proton positions and dynamics in a small protein by liquid crystal NMR spectroscopy, *J. Am. Chem. Soc. 125*, 9179−9191.
25. Teng, C. L., and Bryant, R. G. (2004) Mapping oxygen accessibility to ribonuclease a using high-resolution NMR relaxation spectroscopy, *Biophys. J. 86*, 1713−1725.
26. Ellena, J. F., Moulthrop, J., Wu, J., Rauch, M., Jaysinghne, S., Castle, J. D., and Cafiso, D. S. (2004) Membrane position of a basic aromatic peptide that sequesters phosphatidylinositol 4,5-bisphosphate determined by site-directed spin labeling and high-resolution NMR, *Biophys. J. 87*, 3221−3233.
27. Sakakura, M., Noba, S., Luchette, P. A., Shimada, I., and Prosser, R. S. (2005) An NMR method for the determination of protein-binding interfaces using dioxygen-induced spin−lattice relaxation enhancement, *J. Am. Chem. Soc. 127*, 5826−5832.
28. Teng, C. L., Hong, H., Kiihne, S., and Bryant, R. G. (2001) Molecular oxygen spin-lattice relaxation in solutions measured by proton magnetic relaxation dispersion, *J. Magn. Reson. 148*, 31−34.
29. Prosser, R. S., Luchette, P. A., and Westerman, P. W. (2000) Using O-2 to probe membrane immersion depth by F-19 NMR, *Proc. Natl. Acad. Sci. U.S.A. 97*, 9967−9971.
30. Luchette, P. A., Prosser, R. S., and Sanders, C. R. (2002) Oxygen as a paramagnetic probe of membrane protein structure by cysteine mutagenesis and F-19 NMR spectroscopy, *J. Am. Chem. Soc. 124*, 1778−1781.
31. Prosser, R. S., and Luchette, P. A. (2004) An NMR study of the origin of dioxygen-induced spin-lattice relaxation enhancement and chemical shift perturbation, *J. Magn. Reson. 171*, 225−232.
32. Bertini, I., Castellani, F., Luchinat, C., Martini, G., Parigi, G., and Ristori, S. (2000) Partial orientation of cytochrome *c* in a lyotropic liquid crystal: Residual H−H dipolar coupling, *J. Phys. Chem. B 104*, 10653−10658.
33. Bertini, I., Luchinat, C., and Parigi, G. (2002) Paramagnetic constraints: An aid for quick solution structure determination of paramagnetic metalloproteins, *Concepts Magn. Reson. 14*, 259−286.
34. Brooks, B. R., Bruccoleri, R. E., Olafson, B. D., States, D. J., Swaminathan, S., and Karplus, M. (1983) CHARMM—a program for macromolecular energy, minimization, and dynamics calculations, *J. Comput. Chem. 4*, 187−217.
35. MacKerell, A. D., Bashford, D., Bellott, M., Dunbrack, R. L., Evanseck, J. D., Field, M. J., Fischer, S., Gao, J., Guo, H., Ha, S., Joseph-McCarthy, D., Kuchnir, L., Kuczera, K., Lau, F. T. K., Mattos, C., Michnick, S., Ngo, T., Nguyen, D. T., Prodhom, B., Reiher, W. E., Roux, B., Schlenkrich, M., Smith, J. C., Stote, R., Straub, J., Watanabe, M., Wiorkiewicz-Kuczera, J., Yin, D., and Karplus, M. (1998) All-atom empirical potential for molecular modeling and dynamics studies of proteins, *J. Phys. Chem. B 102*, 3586−3616.
36. Feller, S. E., Brown, C. A., Nizza, D. T., and Gawrisch, K. (2002) Nuclear overhauser enhancement spectroscopy cross-relaxation rates and ethanol distribution across membranes, *Biophys. J. 82*, 1396−1404.
37. Jorgensen, W. L., Chandrasekhar, J., Madura, J. D., Impey, R. W., and Klein, M. L. (1983) Comparison of simple potential functions for simulating liquid water, *J. Chem. Phys. 79*, 926−935.
38. Fischer, J., and Lago, S. (1983) Thermodynamic perturbation-theory for molecular liquid-mixtures, *J. Chem. Phys. 78*, 5750−5758.
39. Hoover, W. G. (1985) Canonical dynamics—equilibrium phase-space distributions, *Phys. Rev. A 31*, 1695−1697.
40. Darden, T., York, D., and Pedersen, L. (1993) Particle Mesh Ewald—an N.log(N) method for Ewald sums in large systems, *J. Chem. Phys. 98*, 10089−10092.

41. Ryckaert, J. P., Ciccotti, G., and Berendsen, H. J. C. (1977) Numerical-integration of Cartesian equations of motion of a system with constraints—Molecular-dynamics of *n*-alkanes, *J. Comput. Phys. 23*, 327−341.
42. Sankararamakrishnan, R., and Weinstein, H. (2004) Surface tension parameterization in molecular dynamics simulations of a phospholipid-bilayer membrane: Calibration and effects, *J. Phys. Chem. B 108*, 11802−11811.
43. Petrache, H. I., Dodd, S. W., and Brown, M. F. (2000) Area per lipid and acyl length distributions in fluid phosphatidylcholines determined by H-2 NMR spectroscopy, *Biophys. J. 79*, 3172−3192.
44. Marrink, S. J., and Mark, A. E. (2003) Molecular dynamics simulation of the formation, structure, and dynamics of small phospholipid vesicles, *J. Am. Chem. Soc. 125*, 15233−15242.
45. Shinoda, W., Mikami, M., Baba, T., and Hato, M. (2004) Molecular dynamics study on the effects of chain branching on the physical properties of lipid bilayers: 2. Permeability, *J. Phys. Chem. B 108*, 9346−9356.
46. Dill, K. A., and Flory, P. J. (1981) Molecular-organization in micelles and vesicles, *Proc. Natl. Acad. Sci. U.S.A. 78*, 676−680.
47. Wiener, M. C., and White, S. H. (1992) Structure of a fluid dioleoylphosphatidylcholine bilayer determined by joint refinement of X-ray and neutron-diffraction data. 3. Complete structure, *Biophys. J. 61*, 434−447.
48. Prosser, R. S., Luchette, P. A., Westerman, P. W., Rozek, A., and Hancock, R. E. W. (2001) Determination of membrane immersion depth with O-2: A high-pressure F-19 NMR study, *Biophys. J. 80*, 1406−1416.
49. Battino, R., Evans, F. D., and Danforth, W. F. (1968) Solubilities of 7 gases in olive oil with reference to theories of transport through cell membrane, *J. Am. Oil Chem. Soc. 45*, 830.
50. Marsh, D. (2001) Polarity and permeation profiles in lipid membranes, *Proc. Natl. Acad. Sci. U.S.A. 98*, 7777−7782.
51. Subczynski, W. K., Hyde, J. S., and Kusumi, A. (1991) Effect of alkyl chain unsaturation and cholesterol intercalation on oxygen-transport in membranes − a pulse esr spin labeling study, *Biochemistry 30*, 8578−8590.
52. Kowert, B. A., and Dang, N. C. (1999) Diffusion of dioxygen in *n*-alkanes, *J. Phys. Chem. A 103*, 779−781.
53. Bertini, I., and Luchinat, C. (1986) *NMR of Paramagnetic Molecules in Biological Systems*, Benjamin-Cummings, Menlo Park, CA.
54. Bezsonova, I., Evanics, F., Marsh, J., Forman-Kay, J. D., and Prosser, R. S. (2006) Oxygen as a paramagnetic probe of clustering and solvent exposure in folded and unfolded states of an SH3 domain (in preparation).
55. Nieh, M. P., Glinka, C. J., Krueger, S., Prosser, R. S., and Katsaras, J. (2001) SANS study of the structural phases of magnetically alignable lanthanide-doped phospholipid mixtures, *Langmuir 17*, 2629−2638.
56. Vold, R. R., and Prosser, R. S. (1996) Magnetically oriented phospholipid bilayered micelles for structural studies of polypeptides. Does the ideal bicelle exist?, *J. Magn. Reson., Ser. B 113*, 267−271.
57. Nielsen, R. D., Che, K. P., Gelb, M. H., and Robinson, B. H. (2005) A ruler for determining the position of proteins in membranes, *J. Am. Chem. Soc. 127*, 6430−6442.

BI060270F